Supporting Information

On the stiffness, strength and toughness of electrospun nanofibers – effect of flow-induced molecular orientation[a]

Israel Greenfeld, XiaoMeng Sui, H. Daniel Wagner

S1. Nanofiber engineering stiffness constants

We use an aggregate representation[1-2] of the solid nanofiber to estimate the polymer elastic properties. The aggregate consists of randomly dispersed, transversely isotropic unit elements (that is, rigid chain segments), each with a main axis of symmetry 1 and a plane of isotropy 2-3 (Figure 4). The unit element is defined by its five independent elastic stiffness constants (that is, elastic moduli), $E_1, E_2, G_{12}, \nu_{12}, \nu_{23}$, and the direction of its main axis is determined by the segmental orientation O. The unit elements are assumed to be aligned with the 3 axes x, y, z of a global Cartesian system, where x is the nanofiber main axis and y, z are the lateral axes (Figure 4).

The compliance matrix of a unit element is denoted by $\mathbf{S}_x$, when axis 1 is aligned with the x axis (Figure 4). The compliance matrices of the laterally oriented unit elements are obtained by angular transformations of $\mathbf{S}_x$, and are denoted by $\mathbf{S}_y$ (axis 1 aligns with y) and $\mathbf{S}_z$ (axis 1 aligns with z). Given an average segmental orientation O and the corresponding orientation probabilities from equation (20), the compliance matrix of the aggregate, $\mathbf{S}$, is obtained by summing up the compliance matrices of all unit elements (assuming iso-stress):

$$\mathbf{S} = P_x\mathbf{S}_x + P_y\mathbf{S}_y + P_z\mathbf{S}_z = \mathbf{S}_0 + \mathbf{M}O \qquad \text{(S1)}$$

[a] In this Supporting Information, references to figures or equations in the main text are denoted without the prefix S.

$\mathbf{S}_0$ is the compliance matrix of an aggregate with randomly oriented elements ($O = 0$):

$$\mathbf{S}_0 = \tfrac{1}{3}\left(\mathbf{S}_x + \mathbf{S}_y + \mathbf{S}_z\right) \tag{S2}$$

and

$$\mathbf{M} = \tfrac{1}{3}\left(2\mathbf{S}_x - \mathbf{S}_y - \mathbf{S}_z\right) \tag{S3}$$

$\mathbf{S}$ is transversely isotropic, as expected from its axial symmetry, and its components are linearly dependent on the orientation. The five engineering stiffness constants of the nanofiber, $E_x, E_y, G_{xy}, \nu_{xy}, \nu_{yz}$, can be extracted from $\mathbf{S}$. The extreme theoretical values are obtained for $O = 1$:

$$\mathbf{S}_{extreme} = \mathbf{S}_0 + \mathbf{M} = \mathbf{S}_x \tag{S4}$$

The compliance matrix of a unit element, when its main axis coincides with the *x* axis, is given by:

$$\mathbf{S}_x = \begin{bmatrix} \frac{1}{E_1} & \frac{-\nu_{12}}{E_1} & \frac{-\nu_{12}}{E_1} & 0 & 0 & 0 \\ \frac{-\nu_{12}}{E_1} & \frac{1}{E_2} & \frac{-\nu_{23}}{E_2} & 0 & 0 & 0 \\ \frac{-\nu_{12}}{E_1} & \frac{-\nu_{23}}{E_2} & \frac{1}{E_2} & 0 & 0 & 0 \\ 0 & 0 & 0 & \frac{2\left(1+\nu_{23}\right)}{E_2} & 0 & 0 \\ 0 & 0 & 0 & 0 & \frac{1}{G_{12}} & 0 \\ 0 & 0 & 0 & 0 & 0 & \frac{1}{G_{12}} \end{bmatrix} \tag{S5}$$

When the unit element is rotated 90º around the z axis (Figure 4), so that its main axis coincides with the y axis, the compliance matrix is given by $\mathbf{S}_y$, and when the unit element is rotated 90º around the y axis (Figure 4), so that its main axis coincides with the z axis, the compliance matrix is given by $\mathbf{S}_z$:

$$\mathbf{S}_y = \begin{bmatrix} \frac{1}{E_2} & -\frac{\nu_{12}}{E_1} & -\frac{\nu_{23}}{E_2} & 0 & 0 & 0 \\ -\frac{\nu_{12}}{E_1} & \frac{1}{E_1} & -\frac{\nu_{12}}{E_1} & 0 & 0 & 0 \\ -\frac{\nu_{23}}{E_2} & -\frac{\nu_{12}}{E_1} & \frac{1}{E_2} & 0 & 0 & 0 \\ 0 & 0 & 0 & \frac{1}{G_{12}} & 0 & 0 \\ 0 & 0 & 0 & 0 & \frac{2(1+\nu_{23})}{E_2} & 0 \\ 0 & 0 & 0 & 0 & 0 & \frac{1}{G_{12}} \end{bmatrix} \quad \mathbf{S}_z = \begin{bmatrix} \frac{1}{E_2} & -\frac{\nu_{23}}{E_2} & -\frac{\nu_{12}}{E_1} & 0 & 0 & 0 \\ -\frac{\nu_{23}}{E_2} & \frac{1}{E_2} & -\frac{\nu_{12}}{E_1} & 0 & 0 & 0 \\ -\frac{\nu_{12}}{E_1} & -\frac{\nu_{12}}{E_1} & \frac{1}{E_1} & 0 & 0 & 0 \\ 0 & 0 & 0 & \frac{1}{G_{12}} & 0 & 0 \\ 0 & 0 & 0 & 0 & \frac{1}{G_{12}} & 0 \\ 0 & 0 & 0 & 0 & 0 & \frac{2(1+\nu_{23})}{E_2} \end{bmatrix} \quad \text{(S6)}$$

Using equation (S1), the resulting aggregate's compliance matrix is:

$$\mathbf{S} = \begin{bmatrix} S_{11} & S_{12} & S_{12} & 0 & 0 & 0 \\ S_{12} & S_{22} & S_{23} & 0 & 0 & 0 \\ S_{12} & S_{23} & S_{22} & 0 & 0 & 0 \\ 0 & 0 & 0 & 2(S_{22}-S_{23}) & 0 & 0 \\ 0 & 0 & 0 & 0 & S_{66} & 0 \\ 0 & 0 & 0 & 0 & 0 & S_{66} \end{bmatrix} \quad \text{(S7)}$$

with the following 5 independent constants:

$$
\begin{aligned}
S_{11} &= \frac{1}{3}\left[\left(\frac{1}{E_1}+\frac{2}{E_2}\right)+2\left(\frac{1}{E_1}-\frac{1}{E_2}\right)O\right] \\
S_{22} &= \frac{1}{3}\left[\left(\frac{1}{E_1}+\frac{2}{E_2}\right)+\left(-\frac{1}{E_1}+\frac{1}{E_2}\right)O\right] \\
S_{66} &= \frac{1}{3}\left[2\left(\frac{1}{G_{12}}+\frac{1+\nu_{23}}{E_2}\right)+\left(\frac{1}{G_{12}}-2\frac{1+\nu_{23}}{E_2}\right)O\right] \\
S_{12} &= -\frac{1}{3}\left[\left(\frac{2\nu_{12}}{E_1}+\frac{\nu_{23}}{E_2}\right)+\left(\frac{\nu_{12}}{E_1}-\frac{\nu_{23}}{E_2}\right)O\right] \\
S_{23} &= -\frac{1}{3}\left[\left(\frac{2\nu_{12}}{E_1}+\frac{\nu_{23}}{E_2}\right)+2\left(-\frac{\nu_{12}}{E_1}+\frac{\nu_{23}}{E_2}\right)O\right]
\end{aligned}
\tag{S8}
$$

The corresponding stiffness constants, in engineering notation, are:

$$
\begin{aligned}
E_x &= 1/S_{11} \\
E_y &= 1/S_{22} \\
G_{xy} &= 1/S_{66} \\
\nu_{xy} &= -S_{12}/S_{11} \\
\nu_{yz} &= -S_{23}/S_{22}
\end{aligned}
\tag{S9}
$$

Hence, the elastic moduli, normalized by the isotropic moduli, are given by:

$$\begin{aligned}
\frac{E_x}{E_0} &= \frac{S_{110}}{S_{11}} = \frac{1}{1-\alpha_E O} \\
\frac{E_y}{E_0} &= \frac{S_{220}}{S_{22}} = \frac{1}{1+\frac{1}{2}\alpha_E O} \\
\frac{G_{xy}}{G_0} &= \frac{S_{660}}{S_{66}} = \frac{1}{1-\alpha_G O} \\
\frac{\nu_{xy}}{\nu_0} &= \frac{S_{12}}{S_{120}}\frac{S_{110}}{S_{11}} = \frac{1-\alpha_\nu O}{1-\alpha_E O} \\
\frac{\nu_{yz}}{\nu_0} &= \frac{S_{23}}{S_{230}}\frac{S_{220}}{S_{22}} = \frac{1+2\alpha_\nu O}{1+\frac{1}{2}\alpha_E O}
\end{aligned} \tag{S10}$$

where the parameters are:

$$\begin{aligned}
E_0 &= \frac{3E_1E_2}{2E_1+E_2} & \alpha_E &= \frac{2E_1/E_2-2}{2E_1/E_2+1} \\
G_0 &= \frac{3E_2G_{12}}{2E_2+2(1+\nu_{23})G_{12}} & \alpha_G &= \frac{2(1+\nu_{23})G_{12}/E_2-1}{2(1+\nu_{23})G_{12}/E_2+2} \\
\nu_0 &= \frac{2\nu_{12}E_2+\nu_{23}E_1}{2E_1+E_2} & \alpha_\nu &= \frac{E_1/E_2-\nu_{12}/\nu_{23}}{E_1/E_2+2\nu_{12}/\nu_{23}}
\end{aligned} \tag{S11}$$

The three parameters α are positive. The dependent shear modulus in the symmetry plane is given by:

$$\frac{G_{yz}}{G_0} = \frac{S_{440}}{S_{44}} = \frac{1}{1+2\alpha_G O} \tag{S12}$$

or just by $G_{yz} = E_y/[2(1+\nu_{23})]$.

These results are depicted in Figure S1, demonstrating that the main effect of nanofiber stretching is the sharp increase in the longitudinal modulus, whereas the other elastic constants are only mildly affected. Note the decrease in both the lateral tensile modulus and the lateral

shear modulus. These trends generally agree with measurements of the elastic constants in cold drawn polymers under a varying draw ratio, a parameter that corresponds to segmental orientation.[2]

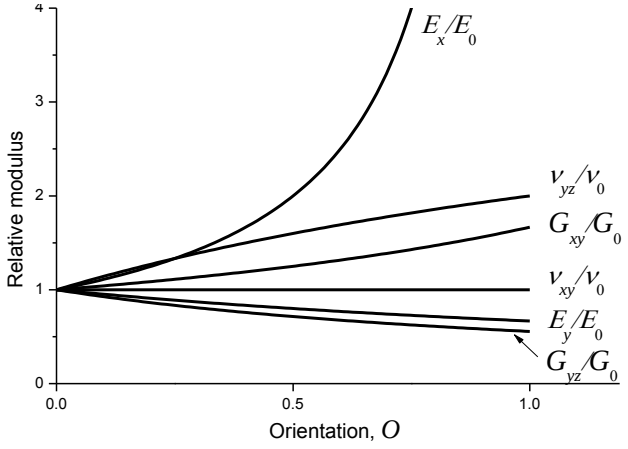

Figure S1: The elastic moduli of the nanofiber aggregate as functions of the molecular orientation O. The following assumptions are used: $E_1 >> E_2$, $G_{12} = E_2$, $\nu_{12} = \nu_{23} = 0.5$, which yield $\alpha_E = 1$, $\alpha_G = 0.4$ and $\alpha_\nu = 1$.

S2. Iso-strain tensile moduli

The analysis in the main text assumes iso-stress condition. For comparison purpose, we calculate here the longitudinal and lateral tensile moduli under iso-strain condition. Instead of summing up the compliances of the aggregate's unit elements, as done for iso-stress, we sum up the stiffnesses in the x and y directions (Figure 4):

$$E_x = P_x E_1 + (P_y + P_z)E_2 = \frac{1}{3}[(E_1 + 2E_2) + (2E_1 - 2E_2)O]$$
$$E_y = P_y E_1 + (P_x + P_z)E_2 = \frac{1}{3}[(E_1 + 2E_2) - (E_1 - E_2)O] \quad \text{(S13)}$$

where the orientation probabilities P_x, P_y, P_z are taken from equation (20). We normalize by the isotropic modulus E_0:

$$\frac{E_x}{E_0} = 1 + \alpha_E O$$
$$\frac{E_y}{E_0} = 1 - \tfrac{1}{2}\alpha_E O \qquad \text{(S14)}$$

where the isotropic modulus is obtained by substituting $O = 0$ in equation (S13):

$$E_0 = \frac{E_1 + 2E_2}{3} \cong \tfrac{1}{3} E_1 \qquad \text{(S15)}$$

and α_E is an engineering constant slightly smaller than 2:

$$\alpha_E = \frac{2E_1/E_2 - 2}{E_1/E_2 + 2} \cong 2 \qquad \text{(S16)}$$

The maximum theoretically achievable longitudinal modulus occurs when $O = 1$ and equals E_1, yielding:

$$\left(\frac{E_x}{E_0}\right)_{\max} = \frac{3E_1/E_2}{E_1/E_2 + 2} \cong 3 \qquad \text{(S17)}$$

Similarly, the minimum theoretical lateral modulus is:

$$\left(\frac{E_y}{E_0}\right)_{\min} = \frac{3}{E_1/E_2 + 2} \cong 0 \qquad (18)$$

These predictions provide an unrealistically high value for E_0 and consequently an unrealistically low value for the modulus rise $(E_x/E_0)_{\max}$, even though $E_{x\max} = E_1$ as in the iso-stress case (equation (27)). The iso-strain predictions are not in the ballpark of experimental

evidence, and are therefore not used. However, we may consider using the iso-stress derived modulus rise as an upper bound, and the iso-strain modulus rise as a lower bound. Because the experimental results in Figure 7 do not seem to approach high saturation of the longitudinal modulus, it is currently impossible to assess whether the upper bound can be approached in practice.

S3. Diameter dependence of elongation

Assuming the maximum strain (that is, elongation) ε_L scales as the probability P_x that a monomer will be aligned with the longitudinal axis, we obtain:

$$\varepsilon_L \approx P_x \approx \frac{1+2O}{3} \approx 1-\frac{1}{3}\left(\frac{D}{D_c}\right)^2 \qquad \text{(S19)}$$

where equation (20) was used for the probability. The right term is for diameters smaller than the critical diameter, using the approximation $O \cong 1-\left(D/D_c\right)^2/2$. According to this theoretical result, the maximum possible elongation ($O=1$) is three times larger than the isotropic elongation ($O=0$).

Equation (S19) generally conforms (with a scaling factor) to the experimental data on elongation provided by Sui et al[3-4], depicted in Figure S2. We see that the elongation rises moderately when the fiber diameter decreases, and eventually saturates at a constant value below 1 (that is, 100% elongation). Similar saturation can be seen also in electrospun PAN nanofibers.[5] Note that the experimental data is widely scattered, both in the large and small diameter domains, possibly an indication for additional failure mechanisms driven by defects. Such defects can arise from free volume regions between polymer chains, or from larger scale pores caused by the rapid evaporation typical of electrospinning.

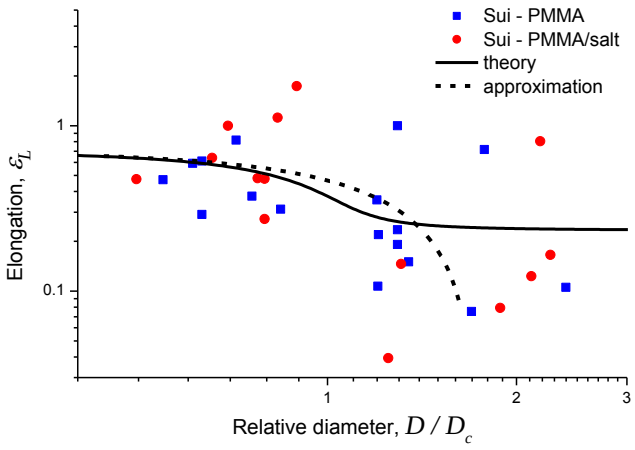

Figure S2: Dependence of the maximum elongation on the relative diameter D/D_c. The experimental data is imported from the study published by Sui et al.[3-4] The critical diameters used to normalized each data set are as in Figure 7. The theoretical solution (solid line) and theoretical approximation (dash line) are given by equation (S19), with initial extension $\varepsilon_0 = 0.1$ and a scaling factor 0.7.

S4. Effect of reinforcing filler

The addition of a tubular filler such as carbon nanotubes (CNTs) to the electrospinning polymer solution reinforces the nanofibers. Under iso-strain conditions, the elastic tensile modulus of the composite nanofiber is given by:[2]

$$E_x^c = \eta_l v_f E_f + (1 - v_f) E_x \qquad \text{(S20)}$$

where E_f and E_x are the filler and polymer longitudinal moduli, v_f is the filler volume fraction, and η_l is a correction factor introduced by shear-lag theory[6] to account for the finite filler length. η_l varies between zero and one, and depends on the composite and its components' structural features.[7] The filler is assumed to be aligned with the nanofiber longitudinal axis, as indeed observed in experiments.[8]

Given the polymer's average segmental orientation O, and normalizing by the polymer

isotropic modulus E_0, we get (using equation (S10)):

$$\frac{E_x^c}{E_0} = \frac{\eta_l v_f E_f}{E_0} + \frac{1 - v_f}{1 - \alpha_E O} \tag{S21}$$

where E_0 and α_E are given by equation (S11). This equation, with O expressed in terms of the relative diameter D/D_c, is depicted in Figure S3 for several values of v_f.

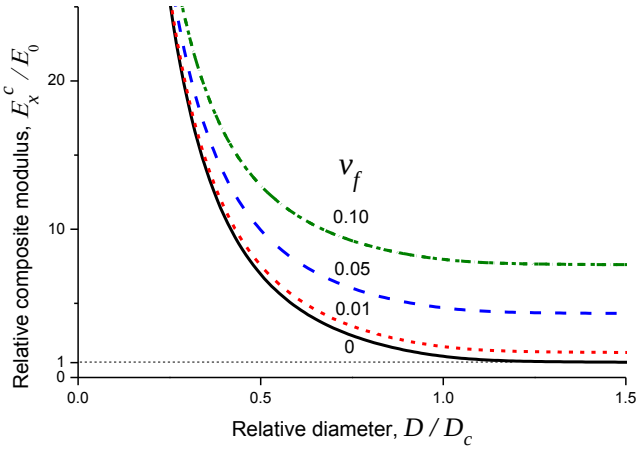

Figure S3: Dependence of the composite's relative longitudinal modulus E_x^c / E_0 on the relative diameter D/D_c, for four values of the filler volume fraction v_f, where E_0 is the polymer isotropic modulus and D_c is the critical diameter. Based on equation (S21), with $\eta_l = 0.5$, initial chain extension $\varepsilon_0 = 0.1$, and $E_f = E_1 = 200E_2$, where E_f is the filler longitudinal modulus, and E_1 and E_2 are the longitudinal and transverse moduli of a polymer chain element.

We can see that before the onset of significant orientation ($O \cong 0$ or $D > D_c$), the filler contribution to the composite modulus is dominant ($E_f >> E_0$), even at relatively low volume fractions. However, upon significant orientation ($O \to 0$ or $D << D_c$), the polymer consists mostly of longitudinally aligned chain segments, each with a modulus comparable[9-10] to that of

the filler (CNT modulus is ~1 TPa)[11-12]. In other words, $E_f \approx E_1$ because both filler and polymer chains consist of straight, covalent-bonded carbon backbones. Therefore, at high segmental orientation, the filler contribution to the composite modulus is not expected to be significant. A similar analysis can be shown for the composite strength as well.

This description is in general agreement with experiments carried out by Sui et al,[3] using electrospun PMMA nanofibers reinforced by multiwall carbon nanotubes (MWCNTs) at ~1% volume fraction, and tested for a range of fiber diameters. These experimental results are compared with those of non-reinforced nanofibers[4] and presented in Figure S4. Although the expected modulus rise for such a low filler concentration is relatively small (~20%), as demonstrated in Figure S3, there is indeed a comparable modulus improvement in the tested nanofibers with large diameters, as well as a similar improvement in the strength. At the small diameters, as predicted above, there is no distinct difference between the moduli or strengths of the reinforced and non-reinforced fibers, even though these properties have risen 5-10 folds with respect to their isotropic counterparts. The PMMA experimental data also includes toughness, showing an improvement by approximately a factor of ~2.5 at small diameters, while almost none observable at the large diameters. A possible explanation for this opposite trend (compared to the modulus and strength trend) relates to the filler toughening mechanism – the energy absorbed during nanofiber fracture by filler pullout from the polymer matrix. For a non-continuous filler, this energy is known to be proportional to the matrix interfacial strength,[7] which, as shown in equation (42) and Figure 8, rises sharply at small diameters.

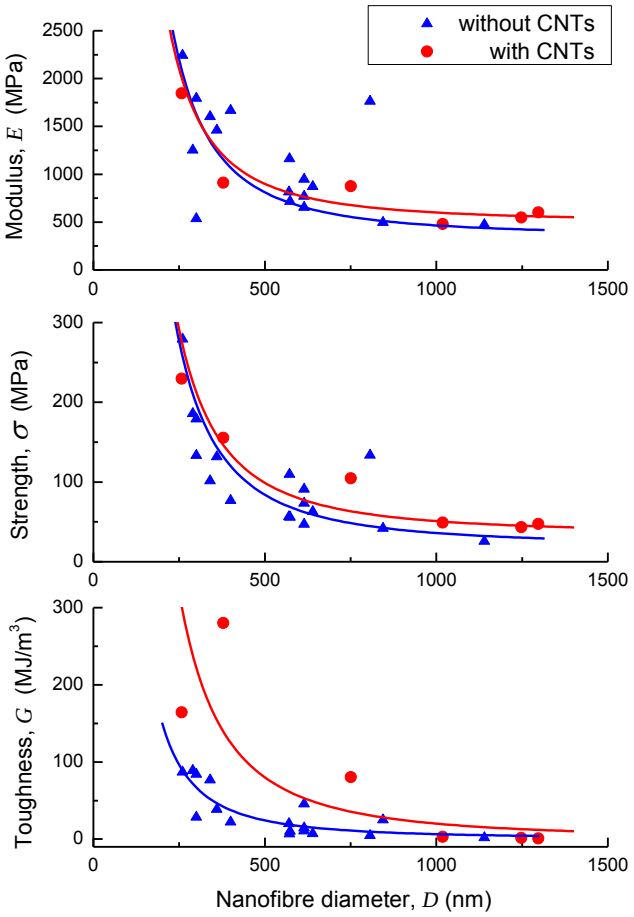

Figure S4: Nanofibers longitudinal elastic modulus E, strength σ, and toughness G versus their diameter D, with and without reinforcement by MWCNTs. The CNTs volume fraction is ~1%. The data is based on experiments of electrospun PMMA nanofibers (Sui et al).[3-4] The lines are fits to equation (S21).

Another interesting experimental observation is provided by Ji et al,[13] using electrospun PS nanofibers reinforced by multiwall carbon nanotubes (MWCNTs) at ~2% volume fraction, and compared with non-reinforced nanofibers. Although no modulus improvement is seen at large diameters, the modulus plot of the reinforced nanofibers is shifted toward larger diameters with respect to the non-reinforced polymer case, by a factor of about three. Ji relates this change to enhanced molecular orientation due to confinement induced by the CNTs, effectively 'dividing' the nanofiber into 2-3 separate regions, each with a fraction of the nanofiber diameter. In terms of

the present paper, we can say that the onset of high orientation in the reinforced case occurred at a larger critical diameter, possibly as a result of reduced jet strain rate caused by the addition of CNTs (see equation (33)).

S5. Dependence on electrospinning process parameters

The relative strain rate s/s_c, and consequently the tensile modulus, can be expressed in terms of the electrospinning process parameters. Theoretical derivation based on jet rheology yields (in CGS electrostatic units):[14-17]

$$s \cong \varepsilon_m^{1/3} D_0^{1/3} \sigma_e^{1/2} \eta^{-5/6} v_0^{-1/3} \mathrm{E}^{5/3} \tag{S22}$$

where $\varepsilon_m \cong 1$ is the permeability of the medium (air), D_0 is the injection diameter, σ_e is the solution electric conductivity, η is the solution viscosity, v_0 is the jet initial velocity, and E is the electric field intensity (not to be confused with the modulus E). The solution viscosity can be expressed by $\eta \cong \eta_s \eta_{sp}$, where η_s is the solvent viscosity, $\eta_{sp} \approx \left(N^3 / N_{e1}^2\right)\phi^{3/(3\nu-1)}$ is the solution specific viscosity for a good (athermal) solvent and $\eta_{sp} \approx \left(N^3 / N_{e1}^2\right)\phi^{14/3}$ for a θ-solvent, and $\eta >> \eta_s$.[18] N is the degree of polymerization, ϕ is the polymer volume concentration in the solution, and N_{e1} is the number of Kuhn monomers in an entanglement strand in a polymer melt. Substituting into equation (S22):

$$s \cong \varepsilon_m^{1/3} D_0^{1/3} \sigma_e^{1/2} \eta_s^{-5/6} N_{e1}^{5/3} N^{-5/2} v_0^{-1/3} \mathrm{E}^{5/3} \begin{cases} \phi^{-\frac{5}{2(3\nu-1)}} & \text{good solvent} \\ \phi^{-35/9} & \theta\text{-solvent} \end{cases} \tag{S23}$$

Using the critical strain rate $s_c = 3\tau^{-1}$ from equation (14) and the chain relaxation time $\tau \approx \tau_0 N^2 \phi^{(1-\nu)/(3\nu-1)}$ from equation (6):

$$\frac{s}{s_c}=\frac{s\tau}{3}\approx\frac{b^3{\varepsilon_m}^{1/3}D_0^{1/3}\eta_s^{1/6}N_{e1}^{5/3}\sigma_e^{1/2}\mathrm{E}^{5/3}}{3k_BTv_0^{1/3}N^{1/2}}\begin{cases}\phi^{-\frac{2\nu+3}{2(3\nu-1)}} & \text{good solvent}\\ \phi^{-26/9} & \theta\text{-solvent}\end{cases} \tag{S24}$$

where $\tau_0\approx\eta_s b^3/(k_BT)$ is the relaxation time of a single monomer,[18] b is the monomer length, k_B is Boltzmann constant, and T is the temperature. Constants of order unity were omitted. The exponents of ϕ are close, -2.73 for a good (athermal) solvent and -2.89 for a θ-solvent, meaning that the dependence of the relative strain rate on the solvent condition should be moderate within the domain theta-good-athermal.

Equation (S24) allows us to characterize the process tradeoffs that may be needed for achieving improved mechanical properties. Using the crossover condition $s=s_c$, and focusing on the concentration, electric field, degree of polymerization, and solvent condition, we obtain the condition for improved properties:

$$\phi<\begin{cases}\left(\mathrm{E}/\mathrm{E}_0\right)^{0.610}N^{-0.183} & \text{good solvent}\\ \left(\mathrm{E}/\mathrm{E}_0\right)^{0.577}N^{-0.173} & \theta\text{-solvent}\end{cases} \tag{S25}$$

where the electric field E is normalized by the scaling factor E_0, which contains the rest of the parameters in Equation (S24):

$$\mathrm{E}_0=\left(\frac{b^3{\varepsilon_m}^{1/3}D_0^{1/3}\eta_s^{1/6}N_{e1}^{5/3}\sigma_e^{1/2}}{3k_BTv_0^{1/3}}\right)^{-5/3} \tag{S26}$$

This condition is depicted in Figure S5. For example, given the polymer molar mass and the solution concentration, we need to select a sufficiently high electric field intensity so that the corresponding line is above the $\phi-N$ point. If the polymer molar mass is increased, the solution concentration should be decreased and/or the electric field increased. Of-course, the selection of parameters is subject to electrospinnability bounds,[16] to ensure formation of a continuous jet.

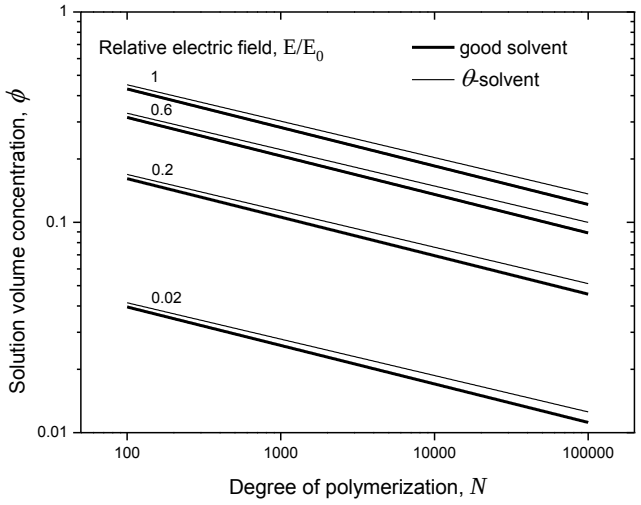

Figure S5: Mapping of the crossover condition for improved mechanical properties (equation (S25)). The improved properties are obtained below the relevant line. To convert N to molar mass M_w multiply by the mass of a single Kuhn monomer, m_0 (typically of order 10^2).

S6. Effects of solvent evaporation and network deformation

The combination of strong jet extension and rapid solvent evaporation, characteristic of the electrospinning process, is the key to the improved mechanical properties of nanofibers. When the jet strain rate is sufficiently high ($s > s_c$), stretching induces a steady high molecular orientation. At the same time, partial solidification by evaporation freezes this non-equilibrium molecular conformation, which otherwise would relax back to an equilibrium randomly oriented conformation. Although some chain relaxation may occur in the partially or fully solidified nanofiber after the jet reaches the collector and the stress is relieved, it is limited by intermolecular interactions, and therefore the high orientation essentially remains.

As shown by our model, chains reach a steady state extension within a time constant inversely proportional to the jet strain rate (equation (7) and Figure 2), in the order of 10^{-5}-10^{-3} s, close to the jet start. In that region, the effect of evaporation is still negligible, and therefore the volume conservation assumption is valid. The onset of significant evaporation at the later stage of

the process decreases the mobility of chains, but the high degree of extension and hence molecular orientation is already there, and the consequential effect of further evaporation is to solidify that conformation.

That said, evaporation gradually increases the polymer volume fraction in the electrospinning solution, and may consequently affect the model. In high stretching, strand extension depends predominantly on a single parameter, $s\tau$, and negligibly on ε_0 (equation (13) and Figure 3). The model's scaling concept, that is the scaling dependence of the orientation, modulus and diameter on $s\tau$ (or equivalently, on s/s_c), is not affected. However, the values of the two components, s and τ, could be affected by the change in polymer concentration ϕ.

The strain rate scales as $s \propto \phi^{-3.3}$ (equation (S23), good solvent), and therefore the gradual rise in the concentration along the jet could possibly decrease the strain rate, and consequently reduce the stabilized chain extension to a lower degree (equation (13) and Figure 3). However, such a moderating effect on the strain rate was not observed, and theoretical and experimental evidence show that the strain rate remains high and even increases significantly when the jet enters the bending (whipping) instability stage.[19-21] These models show that, although the downward velocity stabilizes, the jet curvilinear draw ratio keeps growing with the increasing whipping diameter.

The model by Yarin et al[20] also incorporates evaporation and solidification effects, including mass transfer due to evaporation, vapor diffusion in air, gravity, and solution viscosity changes, and shows that a new higher and fairly constant strain rate sets in upon the onset of instability. For example, in smaller diameter jets, evaporation is more rapid due to the larger surface to volume ratio, but at the same time the draw ratio is higher because of a larger whipping amplitude.[22] Based on these observations, we find that a high strain rate at the initial stage of the jet would essentially remain throughout the jet and even increase, and therefore the stretch model should be valid throughout the jet path. In that respect, equation (S23) should be regarded as the stain rate's scaling relationship with the electrospinning parameters, and the polymer volume fraction parameter could be justifiably regarded as the solution's initial concentration rather than

a varying concentration.

The relaxation time scales as $\tau \propto \phi^{0.54}$ (equation (6), good solvent), and therefore the gradual rise in the concentration could moderately increase the relaxation time, and consequently increase the stabilized chain extension (equation (13) and Figure 3). However, the rising concentration should not have a significant effect, because the relaxation time quickly tends to the steady value of the Rouse relaxation time:

$$\tau \approx \tau_R \approx \tau_0 N^2 \tag{S27}$$

Moreover, although both the relative diameter (equation (34)) and relative modulus (equation (29)) are sensitive to changes in polymer volume fraction and strain rate, their scaling relationship $E_x / E_0 \approx \left(D / D_c\right)^{-2}$ is independent of the concentration and strain rate (equation (35)). The agreement of this relationship with wide and diverse experimental data (Figure 7) provides further substantiation to the scaling approach of the model.

The strong network deformation and the rapid solvent evaporation also result in structural nonuniformity in the radial direction of the jet or nanofiber. In addition to the longitudinal strain rate s, the jet exhibits a corresponding radial strain rate $-s/2$.[23] Using equation (7) and (11) in the radial direction, for a tube whose average orientation coincides with the jet axis:

$$-\frac{s}{2}\tau\varepsilon_r \cong f(\varepsilon_r) - f(\varepsilon_0) \tag{S28}$$

where ε_r is the relative extension in the radial direction. Because this deformation causes compression and results in small values of ε_r, we can substitute $f(\varepsilon) \cong 3\varepsilon$ and get the radial extension:

$$\varepsilon_r \cong \frac{\varepsilon_0}{1 + s\tau/6} \cong \frac{6\varepsilon_0}{s\tau} \quad \text{due to hydrodynamic compression} \tag{S29}$$

where the right term is for high extensions. At the same time, an entanglement strand's high

longitudinal extension is accompanied by its radial compacting due to redistribution of the monomers orientational probabilities. This radial extension component can be derived from equations (16)-(18), yielding $\varepsilon_r \cong 3\varepsilon_0\sqrt{1-\varepsilon^2}$ for high extensions and small ε_0. Substituting ε from equation (13) we get:

$$\varepsilon_r \cong \frac{3\sqrt{2}\varepsilon_0}{\sqrt{s\tau}} \quad \text{due to longitudinal extension} \tag{S30}$$

The ratio between the extension caused by the longitudinal stretching and the extension caused by the radial hydrodynamic compression scales as $\sqrt{s\tau}$, leading to the conclusion that at high extensions the radial hydrodynamic effect becomes negligible, whereas the radial effect associated with the longitudinal extension is dominant. As a result, the stretched polymer network tends to be narrower than the jet diameter, or, in terms of mass transport, the polymer moves inward toward the jet center, leaving the solution closer to the boundary more solvent rich and less entangled. This result was demonstrated theoretically[24-26] and confirmed experimentally[15, 27-28]: X-ray imaging of electrospinning jets exhibited higher polymer concentration in the jet central region; near-field optical imaging of MEH-PPV nanofibers exhibited higher longitudinal molecular orientation in the nanofiber central region; and AFM elastic modulus measurements in nanofibers' cross sections exhibited a higher stiffness in the center.

This analysis demonstrates that the high strain rate leading to the stretch transition and modulus rise is effective throughout the jet, even in the presence of rapid evaporation. The variations in strain rate during the process, particularly a rise when bending instability sets in, have no effect on the scaling properties of the model. Similarly, changes in the confining tube characteristics due to large network deformation[29-30] may affect the macro properties of the flow, but should not have an effect on the model's scaling properties. The radial hydrodynamic effects are negligible with respect to the dominant radial compacting caused by the high longitudinal extension, which, as shown by the model, occurs at an early stage of the jet, prior to the onset of significant evaporation. Consequently, mass transport due to evaporation should not impact the

already compact network. Finally, the validity of the model is also backed by its good agreement with the modulus and strength experimental data.

References

(1) Arridge, R. G. C., *Mechanics of polymers*. Clarendon Press: Oxford [Eng.], 1975; p ix, 246 p.

(2) Ward, I. M.; Sweeney, J., *An introduction to the mechanical properties of solid polymers*. 2nd ed.; Wiley: Chichester, West Sussex, England, 2004; p x, 382 p.

(3) Sui, X. M.; Wagner, H. D. Tough Nanocomposites: The Role of Carbon Nanotube Type. *Nano Letters* **2009,** 9, (4), 1423-1426.

(4) Sui, X. M.; Wiesel, E.; Wagner, H. D. Enhanced Mechanical Properties of Electrospun Nano-Fibers Through NaCl Mediation. *J Nanosci Nanotechno* **2011,** 11, (9), 7931-7936.

(5) Papkov, D.; Zou, Y.; Andalib, M. N.; Goponenko, A.; Cheng, S. Z. D.; Dzenis, Y. A. Simultaneously Strong and Tough Ultrafine Continuous Nanofibers. *Acs Nano* **2013,** 7, (4), 3324-3331.

(6) Cox, H. L. The elasticity and strength of paper and other fibrous materials. *Brit. J. Appl. Phys.* **1952,** 3, 72.

(7) Greenfeld, I.; Wagner, H. D. Nanocomposite toughness, strength and stiffness - the role of filler geometry. *Nanocomposites* **2015,** 1, 3-17.

(8) Richard-Lacroix, M.; Pellerin, C. Molecular Orientation in Electrospun Fibers: From Mats to Single Fibers. *Macromolecules* **2013,** 46, (24), 9473-9493.

(9) Ashby, F.; Jones, D. R. H., *Engineering Materials 1: An Introduction to Properties,*

Applications and Design. Butterworth-Heinemann: 2011; p 496.

(10) Ashby, M. F.; Shercliff, H.; Cebon, D., *Materials: engineering, science, processing and design; North American Edition*. 3rd ed.; Butterworth-Heinemann: 2013.

(11) Wong, E. W.; Sheehan, P. E.; Lieber, C. M. Nanobeam mechanics: Elasticity, strength, and toughness of nanorods and nanotubes. *Science* **1997,** 277, (5334), 1971-1975.

(12) Nardelli, M. B.; Yakobson, B. I.; Bernholc, J. Brittle and ductile behavior in carbon nanotubes. *Phys. Rev. Lett.* **1998,** 81, (21), 4656-4659.

(13) Ji, Y.; Li, C.; Wang, G.; Koo, J.; Ge, S.; Li, B.; Jiang, J.; Herzberg, B.; Klein, T.; Chen, S.; Sokolov, J. C.; Rafailovich, M. H. Confinement-induced super strong PS/MWNT composite nanofibers. *EPL* **2008,** 84, (5), 56002.

(14) Reznik, S. N.; Zussman, E. Capillary-dominated electrified jets of a viscous leaky dielectric liquid. *Phys. Rev. E* **2010,** 81, (2), 026313.

(15) Greenfeld, I.; Fezzaa, K.; Rafailovich, M. H.; Zussman, E. Fast X-ray Phase-Contrast Imaging of Electrospinning Polymer Jets: Measurements of Radius, Velocity, and Concentration. *Macromolecules* **2012,** 45, (8), 3616-3626.

(16) Greenfeld, I.; Zussman, E. Polymer entanglement loss in extensional flow: evidence from electrospun short nanofibers. *J. Polym. Sci., Part B: Polym. Phys.* **2013,** 51, (18), 1377–1391.

(17) Higuera, F. J. Stationary viscosity-dominated electrified capillary jets. *J Fluid Mech* **2006,** 558, 143-152.

(18) Rubinstein, M.; Colby, R. H., *Polymer physics*. Oxford University Press: Oxford ; New York, 2003; p xi, 440 p.

(19) Reneker, D. H.; Yarin, A. L.; Fong, H.; Koombhongse, S. Bending instability of electrically charged liquid jets of polymer solutions in electrospinning. *J. Appl. Phys.* **2000,** 87, (9), 4531-4547.

(20) Yarin, A. L.; Koombhongse, S.; Reneker, D. H. Bending instability in electrospinning of nanofibers. *J. Appl. Phys.* **2001,** 89, (5), 3018-3026.

(21) Reneker, D. H.; Yarin, A. L.; Zussman, E.; Xu, H. Electrospinning of nanofibers from polymer solutions and melts. *Adv. Appl. Mech.* **2007,** 41, 43-195.

(22) Pai, C. L.; Boyce, M. C.; Rutledge, G. C. Mechanical properties of individual electrospun PA 6(3)T fibers and their variation with fiber diameter. *Polymer* **2011,** 52, (10), 2295-2301.

(23) McKinley, G. H.; Sridhar, T. Filament-stretching rheometry of complex fluids. *Annu Rev Fluid Mech* **2002,** 34, 375-415.

(24) Greenfeld, I.; Arinstein, A.; Fezzaa, K.; Rafailovich, M. H.; Zussman, E. Polymer dynamics in semidilute solution during electrospinning: A simple model and experimental observations. *Phys. Rev. E* **2011,** 84, (4), 041806.

(25) Greenfeld, I.; Zussman, E., Polymer Network Dynamics during Electrospinning: Random Walk Simulation. In *Electrospinning: Principles, Practice and Possibilities*, Mitchell, G. R., Ed. The Royal Society of Chemistry: 2015; pp 71-99.

(26) Greenfeld, I.; Zussman, E., Controlling the Nanostructure of Electrospun Polmeric Fibers. In *Electrospinning for High Performance Sensors*, Macagnano, A.; Zampetti, E.; Kny, E., Eds. Springer International Publishing: 2015; pp 35-64.

(27) Camposeo, A.; Greenfeld, I.; Tantussi, F.; Pagliara, S.; Moffa, M.; Fuso, F.; Allegrini, M.; Zussman, E.; Pisignano, D. Local Mechanical Properties of Electrospun Fibers Correlate to Their

Internal Nanostructure. *Nano Letters* **2013,** 13, (11), 5056-5062.

(28) Camposeo, A.; Greenfeld, I.; Tantussi, F.; Moffa, M.; Fuso, F.; Allegrini, M.; Zussman, E.; Pisignano, D. Conformational evolution of elongated polymer solutions tailors the polarization of light-emission from organic nanofibers. *Macromolecules* **2014,** 47, (14), 4704−4710.

(29) Rubinstein, M.; Panyukov, S. Elasticity of polymer networks. *Macromolecules* **2002,** 35, (17), 6670-6686.

(30) Graham, R. S.; Likhtman, A. E.; McLeish, T. C. B. Microscopic theory of linear, entangled polymer chains under rapid deformation including chain stretch and convective constraint release. *J Rheol* **2003,** 47, (5), 1171-1200.